Cell Reports

KCC2 reverse mode helps to clear postsynaptically released potassium at glutamatergic synapses

Graphical abstract

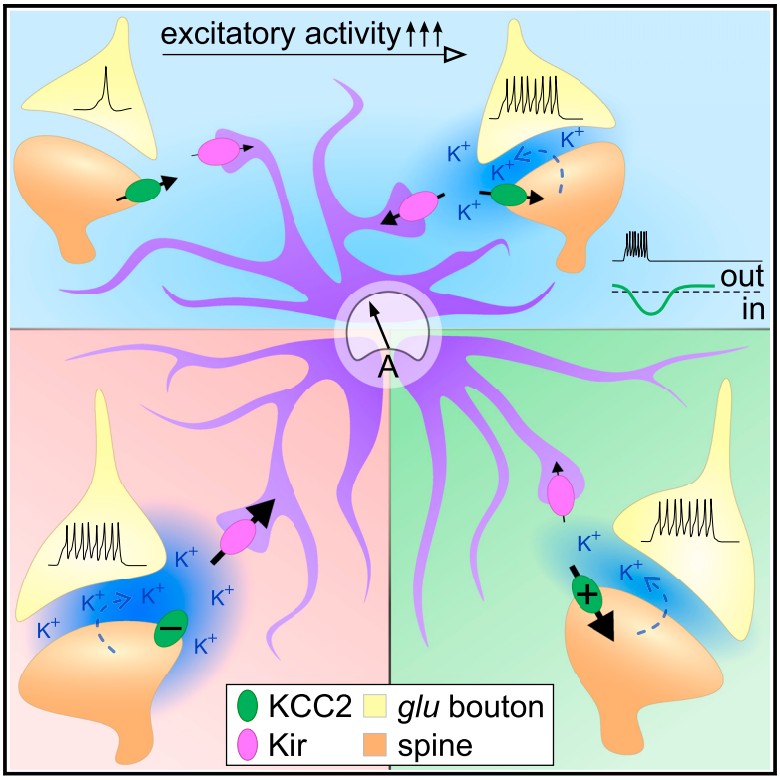

Highlights

- KCC2 is recruited upon perisynaptic K^+ increase due to glutamatergic synaptic activity
- In reverse mode, KCC2 transiently transports perisynaptic K^+ back intothe spine
- KCC2 reversal diminishes perisynaptic K^+, especially when astrocytic K^+ uptake is impaired
- KCC2 reverse mode temporarily restricts presynaptic glutamate release and attenuates LTP

Authors

Egor Byvaltcev, Mahraz Behbood, Jan-Hendrik Schleimer, Thomas Gensch, Alexey Semyanov, Susanne Schreiber, Ulf Strauss

Correspondence

ulf.strauss@charite.de

In brief

Byvaltcev et al. demonstrate a physiological role of KCC2 at dendritic spines by showing KCC2 operation in reverse mode that restricts the perisynaptic potassium increase upon glutamatergic stimulation. They describe KCC2 interactions with other perisynaptic potassium transport mechanisms and the consequences of KCC2 modifications for synaptic signaling.

Byvaltcev et al., 2023, Cell Reports *42*, 112934
August 29, 2023
https://doi.org/10.1016/j.celrep.2023.112934

Cell Reports

CellPress
OPEN ACCESS

Report

KCC2 reverse mode helps to clear postsynaptically released potassium at glutamatergic synapses

Egor Byvaltcev,[1,6] Mahraz Behbood,[2,3,6] Jan-Hendrik Schleimer,[2,3] Thomas Gensch,[4] Alexey Semyanov,[5] Susanne Schreiber,[2,3] and Ulf Strauss[1,7,*]

[1]Charité - Universitätsmedizin Berlin, Institute of Cell- and Neurobiology, Charitéplatz 1, 10117 Berlin, Germany
[2]Institute for Theoretical Biology, Department of Biology, Humboldt-Universität zu Berlin, 10115 Berlin, Germany
[3]Bernstein Center for Computational Neuroscience Berlin, 10115 Berlin, Germany
[4]Institute of Biological Information Processing 1 (IBI-1, Molecular and Cellular Physiology), Forschungszentrum Jülich, Wilhem-Jonen Straße, 52428 Jülich, Germany
[5]Department of Physiology, Jiaxing University College of Medicine, Zhejiang Pro, Jiaxing 314033, China
[6]These authors contributed equally
[7]Lead contact
*Correspondence: ulf.strauss@charite.de
https://doi.org/10.1016/j.celrep.2023.112934

SUMMARY

Extracellular potassium $[K^+]_o$ elevation during synaptic activity retrogradely modifies presynaptic release and astrocytic uptake of glutamate. Hence, local K^+ clearance and replenishment mechanisms are crucial regulators of glutamatergic transmission and plasticity. Based on recordings of astrocytic inward rectifier potassium current I_{Kir} and K^+-sensitive electrodes as sensors of $[K^+]_o$ as well as on *in silico* modeling, we demonstrate that the neuronal K^+-Cl^- co-transporter KCC2 clears local perisynaptic $[K^+]_o$ during synaptic excitation by operating in an activity-dependent reversed mode. In reverse mode, KCC2 replenishes K^+ in dendritic spines and complements clearance of $[K^+]_o$, therewith attenuating presynaptic glutamate release and shortening LTP. We thus demonstrate a physiological role of KCC2 in neuron-glial interactions and regulation of synaptic signaling and plasticity through the uptake of postsynaptically released K^+.

INTRODUCTION

Although large and spatially extended $[K^+]_o$ elevations are long known to cause general neuronal hyperexcitability,[1] local rises in $[K^+]_o$ fulfill a signaling role: e.g., release of K^+ through postsynaptic AMPA and NMDA receptors increases presynaptic release[2] and reduces glutamate uptake by perisynaptic astrocytic leaflets.[3] Narrow space, high tortuosity, local proteome complexity,[4] and low diffusion coefficient restrict the capacity of the perisynaptic extracellular space to buffer $[K^+]_o$ fluctuations during neuronal activity,[5,6] causing increases in $[K^+]_o$, temporarily way beyond physiological levels.[7–9] Outward co-transport of K^+ and Cl^- by neuronal KCC2 may contribute to $[K^+]_o$ when intracellular Cl^- $[Cl^-]_i$ is elevated. So far, research on KCC2 has been mainly focused on this "canonical" outward transport that is linked to synaptic inhibition, keeping $[Cl^-]_i$ at low levels and therewith $GABA_A$ receptor activity hyperpolarizing.[10–15]

Why KCC2 is clustering at dendritic spine heads, i.e., in close vicinity of glutamatergic synapses,[11,14,16] is poorly understood. Even if spine expression is not as high,[17] the presence of KCC2 in places with no particular need for Cl^- gradient control is puzzling and potentially dangerous by leading to neuropathological swelling and blebbing under excitotoxic conditions.[18] Given that functions of KCC2 extend beyond ion translocation in spinogenesis,[19,20] regulation of dendritic spine morphology,[16,21] and actin cytoskeleton,[22,23] a lack of transport activity in this KCC2 "spine pool" has been suggested.[24] We here hypothesize that, even if the ion translocation rate of KCC2 is low in baseline conditions, the rise of $[K^+]_o$ associated with excitatory transmission temporarily facilitates the reverse mode of KCC2 in synapse-rich regions such as *s. radiatum* of CA1. The ability of KCC2 to pump K^+ (and Cl^-) *into* neurons during sudden $[K^+]_o$ rises (e.g., during seizures) has been hypothesized based on considerations that first, ionic co-transport by KCC2 is driven by the K^+ gradient and, second, that KCC2 operates near its reversal under physiological conditions.[25,26] Although such inward transport was implemented in *in silico* models[27] and generally proven possible in cultured midbrain neurons under extreme conditions,[28,29] experimental evidence that inward ionic transport via KCC2 actually occurs in the brain is very recent and sparse.[18] Reasons for this might be the electroneutrality of KCC2 flux that renders direct electrophysiological assessment impossible as well as the relative slowness of Cl^- indicators. Here, we use the astrocytic uptake of $[K^+]_o$ via inward rectifying potassium (K_{ir}) channels to estimate the contribution of KCC2 to $[K^+]_o$ clearance (for details see STAR Methods). Changes in astrocytic I_{Kir} upon KCC2 modulation indicate an inward direction of KCC2 transport at elevated $[K^+]_o$. We complemented this finding with a mathematical model analysis to directly capture biophysical KCC2 and $[K^+]_o$ dynamics and link them to the resulting I_{Kir}. Taken together, both experimental data and modeling provide evidence for a reversal of KCC2 transport direction that, in turn, affects information transmission by excitatory synapses.

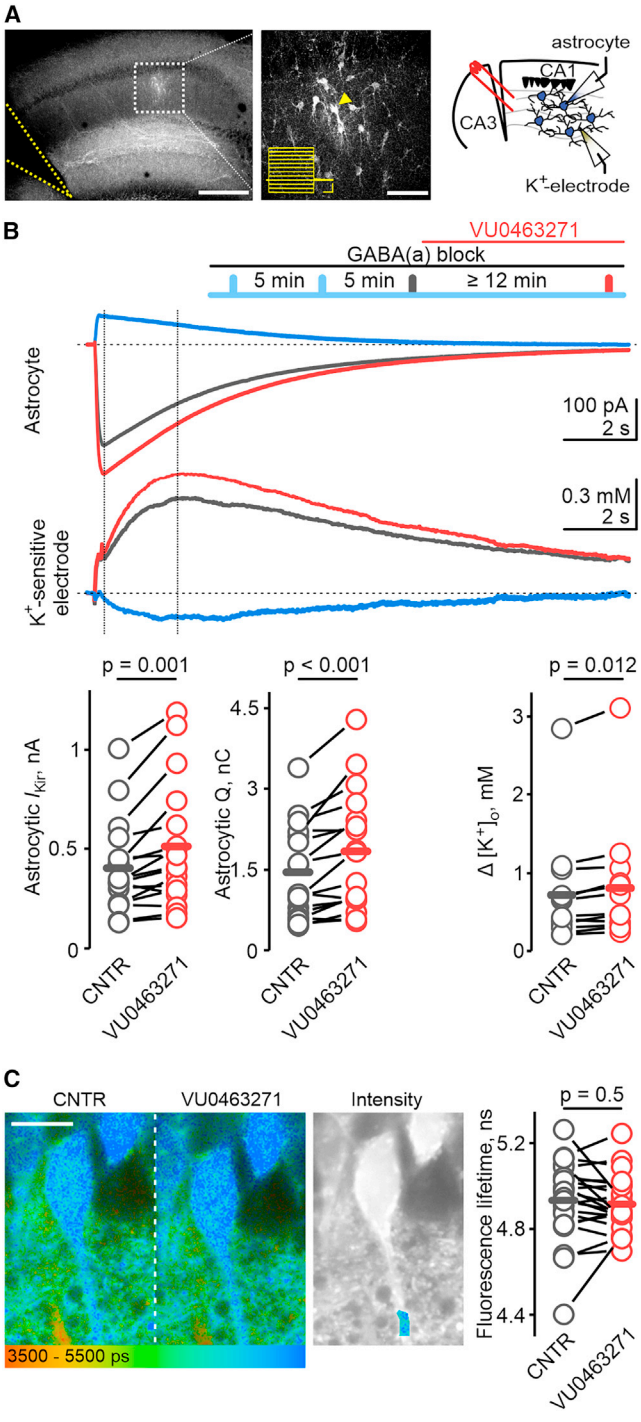

Figure 1. KCC2 inhibition increases transient $[K^+]_o$ elevation elicited by synaptic CA1 excitation

(A) Left: location of biocytin-labeled astrocyte syncytium in hippocampal CA1 *s. radiatum*. Note the cut between CA3/CA1 (dotted yellow lines) to prevent hyperexcitability upon $GABA_AR$ block (scale bar: 200 μm). Middle: close up on astrocyte syncytium (scale bar: 50 μm; inset: voltage response of the recorded astrocyte [arrowhead] to 250 pA current steps, scale bar: horizontal 200 ms, vertical 10 mV). Right: experiment scheme.

(B) The specific KCC2 blocker VU0463271 (10 μM) increased astrocytic K^+ uptake ($I_{Kir\text{-}ctrl}$ = 405 ± 56 pA to $I_{Kir\text{-}VU}$ = 512 ± 77 pA; n = 17, Wilcoxon signed-rank [WSR]; Q_{cntr} = 1,443 ± 212 pC, Q_{VU} = 1,893 ± 270 pC, n = 17, pTT) as well as K^+-sensitive electrode peak voltage (V_{cntr} = 5.8 ± 1.3 mV to V_{VU} = 6.4 ± 1.3 mV, n = 13, WSR) and respective Δ $[K^+]_o$ (Δ$[K^+]_{ocntr}$ = 0.72 ± 0.19 mM to Δ $[K^+]_{oVU}$ = 0.8 ± 0.21 mM, WSR). Top: experiment scheme. Middle: example traces of astrocytic whole-cell current and electrode sensed $[K^+]_o$ deflection without (black) and with VU (red) as well as the difference between the two (blue); scale bars are to the right of the respective trace groups. Bottom: population data.

(C) Blocking KCC2 did not change neuronal $[Cl^-]_i$. Left: color-coded fluorescence lifetime images of CA1 loaded with the Cl^--sensitive dye MQAE without (left) and with VU (middle) and corresponding fluorescence intensity image with marked dendritic region of interest (ROI) (right); scale bar: 10 μm. Lifetime color code scale bar: from 3,500 ps (warm red, high $[Cl^-]_i$) to 5,500 ps (cold blue, low $[Cl^-]_i$). Right: population data of ROI fluorescent lifetime without and with VU ($\tau_{ROI\ dendrite\ cntr}$ = 4.932 ± 0.040 ns vs. $\tau_{ROI\ dendrite\ VU}$ = 4.913 ± 0.028 ns, n = 22, pTT). Line series of population data in this and the following figures connects individual paired recordings before and after treatment. Horizontal bars represent means.

RESULTS

KCC2 modulation reciprocally influenced perisynaptic $[K^+]_o$

Schaffer collateral stimulation triggers substantial release of K^+ from postsynaptic AMPA and NMDA receptors to the synaptic cleft.[2] We raised perisynaptic $[K^+]_o$ by stimulating with 20 pulses at 100 Hz to minimize consequences of stronger excitation such as retraction of astrocytic processes,[30] neuronal Cl^- [18]/Na^+ [31] overload, or axonal depolarization block.[9] This stimulation resulted in I_{Kir} in hippocampal CA1 *s. radiatum* astrocytes (Figure 1A/B). Peak I_{Kir} was neither substantially contaminated by glutamate transporters nor by Na^{2+}-K^+-Cl^- co-transporter (NKCC1) currents[32] (almost completely blocked by Ba^{2+},[33]; Figure S1A). The detected perisynaptic $[K^+]_o$ originated mainly from AMPA/NMDA receptors[2,9,34] because blocking of these receptors greatly reduced I_{Kir}, while $GABA_B$ receptor block did not (Figures S1B and S1C). Relative restriction of $[K^+]_o$ in time and perisynaptic space might be reflected in the delayed and putatively attenuated detection by K^+-sensitive electrodes (Figure 1B). Preconditioning the slices minimized contribution of synaptic potentiation or activity-dependent changes in astrocyte function as controlled by field excitatory postsynaptic potential (fEPSP) and astrocytic responses in long-term recordings (Figures S1D and S1E).

Based on this thorough procedure, we found that neuronal KCC2 substantially contributes to $[K^+]_o$ removal in brain tissue: Firstly, blocking KCC2 by VU0463271 increased I_{Kir} by a good 30% (Figure 1B). KCC2 blocking was efficient irrespective of the type of $GABA_A$ receptor blocker (bicuculline or picrotoxin) that we routinely used to prevent neuronal $GABA_A$ receptormediated $[Cl^-]_i$ increase (Figure S1F). We even detected the effect of KCC2 blockade by K^+-sensitive electrodes that are putatively remote from perisynaptic sites and record in a space averaged manner, obstacles that in sum might contribute to an attenuated $[K^+]_o$ increase upon VU0463271 that amounted to 11% (Figure 1B). Notably, VU0463271 application itself did not change dendritic $[Cl^-]$ (Figure 1C). Secondly, if KCC2 contributes to $[K^+]_o$ clearance, potentiating it should decrease astrocytic I_{Kir}. Closantel, which removes SPS/Ste20-related proline-alanine-rich kinase (SPAK)/oxidative stress response kinase 1 (OSR1) phosphorylation of KCC2 at T907/T1007,[12,15] disinhibits

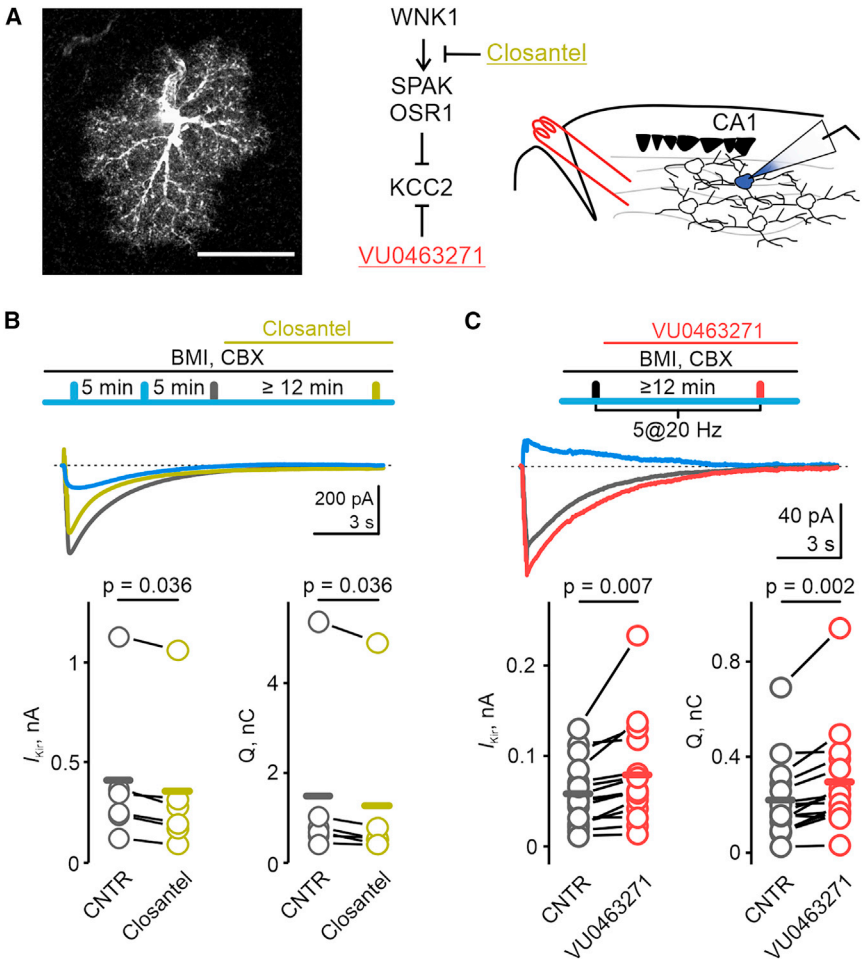

Figure 2. KCC2 modulation affects $[K^+]_o$

(A) Left: biocytin-labeled single *s. radiatum* astrocyte isolated by the gap junction blocker carbenoxolone (CBX); scale bar: 25 μm. Middle: mode of action for VU0463271 and closantel. Right: experiment scheme.

(B) Closantel (10 μM) decreased I_{Kir} in the presence of CBX (100 μM) for >20 min prior to recordings ($I_{Kir\text{-}ctrl}$ = 411 ± 148 pA, $I_{Kir\text{-}Closantel}$ = 355 ± 144 pA; n = 6; Q_{cntr} = 1,491 ± 779 pC, $Q_{Closantel}$ = 1,270 ± 727 pC, n = 6, WSR respectively). Top: experiment timeline. Middle: examples of astrocytic I_{Kir} without (black) and with closantel (gold) traces and the difference between the two (blue); time and current amplitude scale down right. Bottom: population data.

(C) CBX (100 μM) unmasks the VU-mediated (10 μM) increase of I_{Kir} during low-intensity stimulation ($I_{Kir\text{-}ctrl}$ = 58 ± 9 pA, $I_{Kir\text{-}VU0463271}$ 78 ± 14 pA, n = 16, pTT; Q_{cntr}: 219 ± 43 pC, $Q_{VU0463271}$ = 297 ± 56 pC, n = 15; WSR) regardless of intra- or extracellular CBX application (Figure S3). Top: experiment timeline. Middle: examples of astrocytic I_{Kir} without (black) and with VU (red) and the difference between the two (blue); time and current amplitude scale down right. Right bottom: population data.

KCC2. Indeed, closantel decreased I_{Kir} by about 20% (Figure 2A/B) but only when we blocked gap junctions to prevent spatial buffering of K^+ (Figure S2A). In our case, the controversial KCC2 enhancer CLP257[35] did not decrease I_{Kir} (Figure S2B).

We finally checked for factors that might confound our recordings. KCC2 blocking or enhancement did not alter astrocytic I_{Kir} when we directly puffed K^+ (30 mM) to the astrocyte soma or when we blocked glutamatergic transmission (Figure S2C/D). This suggests that neither VU0463271 nor closantel affected extra-synaptic $[K^+]_o$ clearing and that KCC2-mediated $[K^+]_o$ clearance was restricted to local perisynaptic $[K^+]_o$ elevations caused by K^+ efflux upon excitatory transmission. In line, VU0463271 application did not increase the excitability of presynaptic axons (Figures S2E and S2F) under conditions that did not engage KCC2 in $[K^+]_o$ clearance (next paragraph).

Together, these data demonstrate that KCC2 operates in reverse mode helping to clear perisynaptic $[K^+]_o$ during synaptic activity.

Detection of KCC2 reverse mode is activity dependent

So far, we rather strongly excited numerous synapses simultaneously providing substantial perisynaptic $[K^+]_o$ elevation. We next asked whether KCC2 can clear $[K^+]_o$ that results from less intense excitation (5 pulses at 20 Hz) that neither potentiated fEPSP nor changed astrocytic I_{Kir} (Figures S3A and S3B). KCC2 blocking upon such excitation merely tended to increase I_{Kir} (Figure S3C), suggesting that the perisynaptic $[K^+]_o$ rise was insufficient to foster KCC2 reverse mode. To prevent astrocytic spatial K^+ buffering, i.e., to exclude interference of gap junctional dynamics in perisynaptic processes[36] and eliminate leak current,[37] we again perfused slices with carbenoxolone (CBX). With this compromised astrocytic syncytium, the effect of KCC2 blocking became more pronounced (Figure 2C). To minimize side and network effects, we applied CBX through the patch pipette only in the recorded astrocyte (Figure S3D). Under this condition, VU0463271 increased I_{Kir} as under extracellular CBX pre-application. This suggests that under low synaptic activity, K^+ clearance by astrocytes is sufficient when coupled to the syncytium, and KCC2 reversal is not required, i.e., astrocyte coupling regulates recruitment of postsynaptic KCC2. Despite the use of CBX, KCC2 blocking did not change astrocytic I_{Kir} upon a single Schaffer collateral stimulation, suggesting that the expected change was below detection threshold, or KCC2 did not engage in $[K^+]_o$ clearance regardless of its intensity (Figure S3E).

In summary, repetitive synaptic activity prompts KCC2 to act as a substantial sink for perisynaptic $[K^+]_o$. The requirement of repetitive stimulation for a sufficient buildup of local $[K^+]_o$ is in line with the prominent NMDA mediation of spine K^+ efflux.[2]

Kinetics and consequences of KCC2 fluxes revealed by mathematical modeling

Because direct experimental observation of KCC2 ion flux is not currently feasible, we employed a mathematical model of

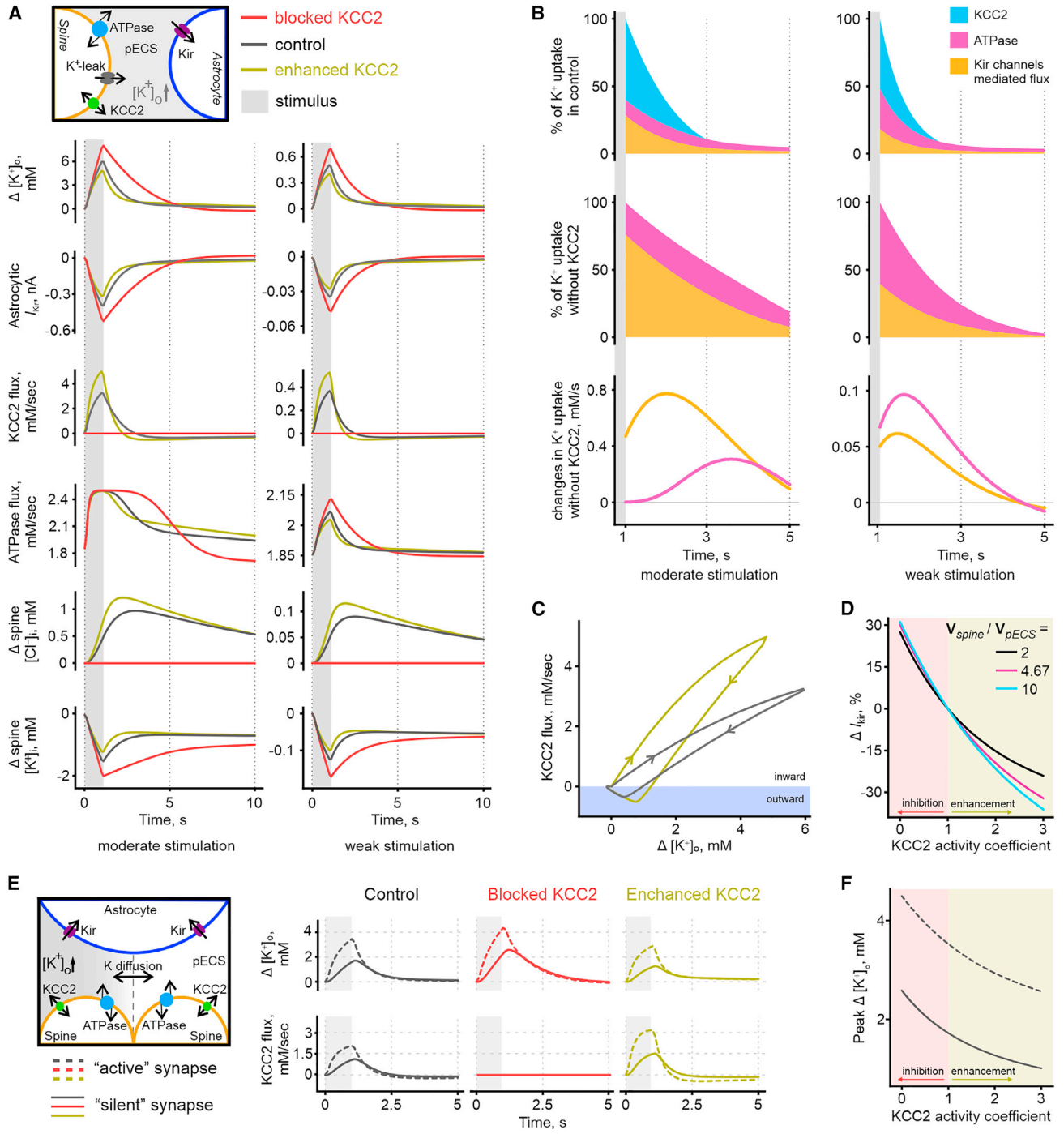

Figure 3. Inferring KCC2 ionic kinetics and fluxes from modeling

(A) KCC2 flux required to mimic astrocytic I_{Kir} changes in our electrophysiological experiments. Top: scheme of the model. Bottom: $[K^+]_o$ increase representing moderate (10 mM/s for 1 s) or weak (1 mM/s for 1 s) synaptic stimulation (gray vertical bar) and consequential changes varying with different strength of KCC2 activity (control: $g_{KCC2} = g_{KCC2\text{-}cntr}$, black; blocked: $g_{kcc2} = 0$, red; and enhanced: $g_{KCC2} = g_{KCC2\text{-}cntr} \times 2$, gold).

(B) Alterations in uptake patterns after stimulation under varying stimulation strengths. Upper and middle row: relative contribution (in percent) of KCC2 (blue), Na/K-ATPase (pink), and K_{ir} channel-mediated (orange) fluxes to the clearance of induced perisynaptic $[K^+]_o$ increase (stimulation) under control conditions and with blocked KCC2, respectively. Baseline activity of each contributor is subtracted to isolate specific changes attributed to the stimulus. Contributions are presented relative to the maximum total clearance flux changes. Lower row: changes in K^+ fluxes via Na/K-ATPase (pink line) and K_{ir} channels (orange line), respectively (depicted is the difference between control and KCC2 block).

(legend continued on next page)

dynamic K^+ and Cl^- exchange between the effective spine, perisynaptic extracellular space (pECS), and astrocyte compartments (see STAR Methods). This approach elucidates the role of KCC2 in $[K^+]_o$ ionostasis. We kept the model simple to fathom minimal biophysical assumptions for the changing direction of KCC2 transport and its temporal dynamics. In this model, $[K^+]_o$ has three determinants: astrocytic I_{Kir}, ion fluxes through neural KCC2 as well as those mediated by the Na/K-ATPase. After a rapid $[K^+]_o$ increase, the equilibrium potential shifts, favoring temporary KCC2 reverse mode and resulting in a considerable uptake of K^+ (co-transported with Cl^-) in the effective spine compartment (corresponding to ≈40% of the modeled $[K^+]_o$ increase upon stimulation). The inflow of Cl^- and drop of $[K^+]_o$ electrochemically leads to a subsequent KCC2 direct mode, which causes a gradual release of potassium from the spine compartment to the pECS compartment through KCC2. The K^+ released is then absorbed by Na/K-ATPase and I_{Kir}. We simulated synaptic activity by adding K^+ from the spine to the pECS. The effect of KCC2 reverse mode is apparent for both weak and moderate stimulation (Figure 3A); however, the small effect for weak stimulation could be masked by other dynamics, such as contribution of the different clearance mechanisms. Indeed, uptake patterns vary with stimulation strength and time after the stimulus (Figure 3B): whereas upon weak stimulation the contribution of I_{Kir} and Na/K-ATPase is comparable with and without KCC2, I_{Kir} contribution is pronounced upon moderate stimulation, in particular without KCC2. This means that I_{Kir} contribution differentially reflects the absence of KCC2, although KCC2 almost equally contributes to the initial uptake of increased perisynaptic $[K^+]_o$ after moderate vs. weak stimulation. The main reason for this is the arrival at maximum Na/K-ATPase capacity with larger stimulus intensity.

The phase plane dynamics of KCC2 against $[K^+]_o$ shows the rapid and high-amplitude inward KCC2 flux when $[K^+]_o$ is elevated and the low-amplitude but persistent outward KCC2 flux when $[K^+]_o$ approximates normal values and spine $[Cl^-]_i$ is elevated (Figures 3C and S4B). Direction of KCC2 mode and efficiency depend on spine and pECS ionic concentrations as well as KCC2 flux capacity (see STAR Methods, Equation 6). Hence, the effect of KCC2 enhancement depends not only on pharmacological agents like closantel (Figure 3D, x axis), but also on the volume ratio (r_{se}) between spine and pECS (Figure 3D). The impact of the ionic flux between spine and the pECS compartment on their ionic concentrations is dictated by r_{se} (see STAR Methods, Equations 1, 9, and 10). When r_{se} is smaller, the enhancement of KCC2 also has a smaller effect. For a portion of spines, r_{se} may be small, explaining the comparably limited effect of pharmacological KCC2 enhancement (Figure 2B).

CA3 to CA1 synapses are only 0.5 μm apart on average,[38] but synaptic spillover due to differential activity between neighboring compartments cannot be addressed experimentally due to a lack of target specificity. While our first simulations employed one large equivalent compartment, we next set out to study spatial K^+ spread. As a simple approximation, we discretized spine and pECS compartments into active and silent sections. The active compartment was stimulated by a flux of K^+ from the spine to pECS compartment. Connection of pECS compartments allowed for K^+ diffusion. KCC2 activity determined the increase of $[K^+]_o$ in both pECS compartments (Figures 3E, 3F,and S4D). The increase of $[K^+]_o$ in neighboring compartments was also controlled by the diffusion time constant (Figure S4C), but the qualitative effect of KCC2 remained in various diffusion timescales.

The mathematical model suggests that (1) KCC2 in reverse mode temporarily dampens $[K^+]_o$ when $[K^+]_o$ rises abruptly, (2) KCC2 reversal can decrease the workload of other homeostatic mechanisms (Na/K-ATPase current and I_{Kir}) during the peak raise of $[K^+]_o$ and distribute the workload over a longer period of time, and (3) KCC2 deficiency increases synaptic K^+ spillover. In complementing the indirect nature of our experimental approach, mathematical modeling shows that inward KCC2 transport suffices to explain our observations under physiologically plausible conditions, strengthening the explanatory power of our hypothesis.

KCC2 smoothens transient peaks in excitatory transmission

Rising $[K^+]_o$ in the synaptic cleft depolarizes the pre-synapse[9] and increases glutamate release probability.[2] Therefore, we hypothesize that KCC2 reciprocally modulates spontaneous (s) EPSCs shortly after Schaffer collateral stimulation in CA1 pyramidal neurons. Blocking KCC2 with VU0463271 increased the frequency of sEPSCs (Figure 4A) with a time course matching the expected KCC2 influence on perisynaptic $[K^+]_o$ (Figure 3A). In contrast, enhancing KCC2 with closantel reduced the sEPSC frequency when we blocked gap junctions to debunk the effect of KCC2 enhancement (Figure 4B). In both cases, sEPSC amplitudes remained comparable. These data support a contributing role for postsynaptic KCC2 in regulating presynaptic excitability. Notably, pharmacological KCC2 blocking did not induce changes in GluR1 clusters as shown previously.[16]

Next, we checked if our stimulation (20 pulses at 100 Hz) revealed differences in LTP upon KCC2 alteration as elegantly reported previously in aged mice and attributed to Cl^- overload and successive depolarizing $GABA_A$ receptor responses.[13] In our slice experiments in young mice, we ruled out $GABA_A$ receptor-mediated Cl^- load or any $GABA_A$ receptor-mediated responses by use of bicuculline and skipped the preconditioning.

(C) Dynamic of KCC2 flux against the difference of $[K^+]_o$ during simulation of control (black) and enhanced (gold) state (based on A, moderate stimulation). KCC2 flux direction at different $[K^+]_o$ depends on spine $[Cl^-]_i$. Note the transient large positive KCC2 influx during and after the stimulus. However, the small negative amplitude persists much longer after reversing the direction (Figure S4A).
(D) Impact of KCC2 modulation depends on the volume ratio of the spine compartment to perisynaptic (pECS) compartment. Diminishing the assumed spine to pECS volume ratio of 4.67 (magenta) to 2 (black) attenuated, while raising it to 10 (cyan) increased the efficiency of KCC2 reverse mode, especially when KCC2 is enhanced.
(E) K^+ spillover from the "active" (dotted) synapse compartment to the "silent" (solid) synapse compartment depends on KCC2 efficiency. Right: time course of parameters in relation to KCC2 activity depicted as in (A). Left: scheme of the extended model. Gray vertical bars indicate $[K^+]_o$ increase (10 mM/s for 1 s).
(F) KCC2 activity influenced the maximum increase of $[K^+]_o$ in both active (dotted) and silent (solid) extracellular compartments.

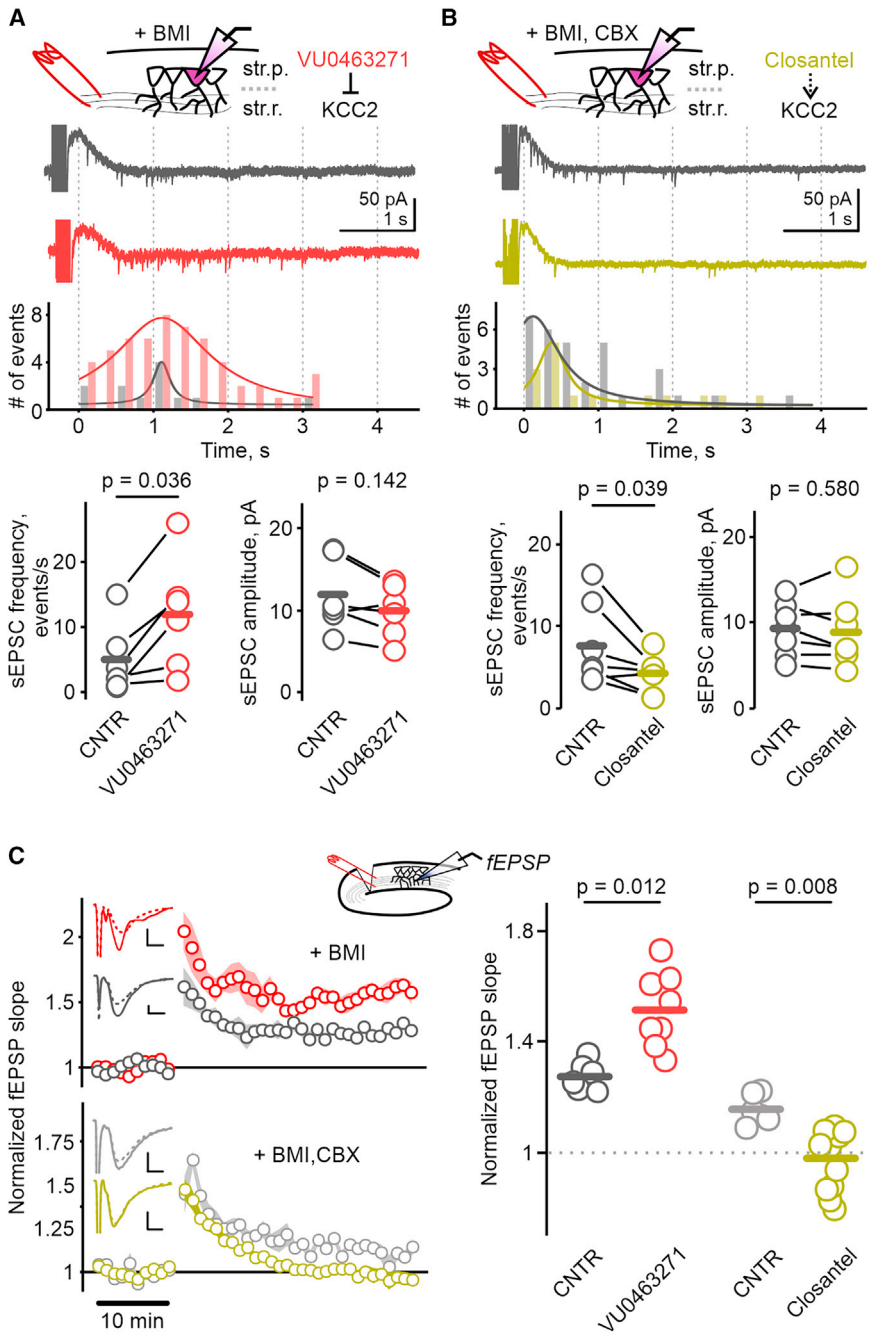

Figure 4. KCC2 alteration uncovers the physiological relevance of inward co-transport

(A) KCC2 inhibition results in increased frequency but not amplitude of early (0–4 s) post-stimulation sEPSC in CA1 pyramidal neurons (f_{ctrl} = 5.0 ± 2.2 events/s, f_{VU} = 12 ± 3.5 events/s, n = 6; $I_{EPSCctrl}$ = 11.9 ± 1.8 pA, I_{EPSCVU} = 9.9 ± 1.3 pA, n = 6). Top: experiment scheme. Middle: neuronal example current traces under control condition (black) and with added VU (red); scale bars on the right between them and binned number of events (bin size = 250 ms, Lorentz curve fitting). Bottom: population data, WSR.

(B) When gap junctions were closed by CBX (100 μM), closantel reduced the frequency of post-stimulation sEPSC in CA1 pyramidal neurons leaving their amplitude unchanged (f_{ctrl} = 7.6 ± 1.9 events/s, $f_{Closantel}$ = 4.1 ± 0.8 events/s, n = 7; $I_{EPSCctrl}$ = 9.2 ± 1.1 pA, $I_{EPSCClosantel}$ = 8.9 ± 1.5 pA, n = 7). Top: experiment scheme. Middle: neuronal example current traces under control conditions (black) and with added closantel (gold); scale bars on the right between them and binned number of events (bin size = 250 ms, Lorentz curve fitting). Note: most sEPSC frequency changes in A/B occurred within 2–3 s after stimulation, mimicking the simulated time course of KCC2 inward transport (Figure 3A). Bottom: population data, pTT.

(C) Synaptic potentiation modulated by KCC2 efficiency. Left: KCC2 blocking augmented LTP (upper panel, VU0463271, red, LTP_{cntr} = 1.27 ± 0.03, n = 6; LTP_{VU} = 1.51 ± 0.06, n = 8, MWT), whereas enhancing KCC2 attenuated LTP (lower panel, closantel, gold, $LTP_{cntr\text{-}CBX}$ = 1.16 ± 0.03, n = 6; $LTP_{Closantel\text{-}CBX}$ = 0.98 ± 0.04, n = 11, MWT) compared to the respective control (black and gray). Insets: averaged fEPSP traces before (dotted) and after (solid) LTP induction. Scale bars: 5 ms, 0.25 mV. Right: population data of fEPSC slopes normalized and averaged (20–30 min after LTP induction).

Under these conditions, blocking of KCC2 elevated and closantel mitigated LTP (Figure 4C). This suggests that KCC2-mediated clearance of transient elevations of $[K^+]_o$ within the perisynaptic compartment interacts with key mechanisms of information storage, even if GABAergic mechanisms are not involved.

DISCUSSION

Interactions among cell types in the brain active milieu underlie proper brain function.[39] Although synaptic and extra-synaptic transmission mediated by neurotransmitters and neuromodulators has been studied for decades, less is known about local ionic signaling. Here, we have addressed the role of the neuronal K^+/Cl^- co-transporter KCC2 in shaping perisynaptic K^+ transients. KCC2 is well appreciated for regulating neuronal transmembrane Cl^- gradients and therewith GABAergic inhibition by extruding $[Cl^-]_i$. A reversal of the transport direction (Cl^-/K^+ influx) has recently been identified as mechanism in excitotoxicity due to long-lasting local $[Cl^-]_i$ overload.[18] We report by electrophysiological means and supported by mathematical modeling that such KCC2 reverse mode occurs under physiological conditions and transiently yet substantially helps to clear K^+ from perisynaptic space to replenish it in the spine. The KCC2 reverse mode required sufficient perisynaptic $[K^+]_o$ elevations that locally sum up in repetitive excitatory signaling,[2] such elevations occurring both in physiological (e.g., brain rhythms) and in pathological conditions (e.g., seizures). Notably, blocking of

astrocytic gap junctions lowered the threshold of KCC2 contribution to K^+ clearance. Thus, we link astrocytic gap junction coupling, KCC2, and K^+ ionostasis in perisynaptic space. A change in astrocytic coupling occurs in dieting,[40] aging,[41] and pathological conditions.[42]

Neuronal KCC2 joins the Na/K-ATPase and astrocytic K_{ir} channels in regulating $[K^+]_o$ and might therewith reduce the peak energy consumption of Na/K-ATPase. Replenishing $[K^+]_i$ in spines eventually enables continued K^+ efflux through AMPA/NMDA receptors.[2] The use of astrocytes as K^+ sensor indicated a reciprocal connection of $[K^+]_o$ and KCC2. Although close by, prompt, and sensitive, in acute brain slice preparations, this method might underestimate the absolute amount of KCC2's contribution to perisynaptic $[K^+]_o$ clearance *in vivo* due to raised neuronal $[Cl^-]_i$ at the slice surface,[43] rendering KCC2 reversal thermodynamically difficult. In addition, astrocytes might not be ideal quantitative sensors due to low membrane input resistance and current loss (up to 30%) through connexins.[37] Regardless of the actual effect size, KCC2 ion flux alterations regulate perisynaptic $[K^+]_o$ and hence directly fine-tune excitatory neurotransmission under non-pathologic conditions. This implies that any mechanism of KCC2 alteration, such as activity-driven KCC2 dispersal,[44] will not only impact $[Cl^-]_i$ and, therefore, $GABA_A$ efficiency. K^+ flux alterations may also partially counteract ion-flux-independent effects of KCC2 changes on the efficiency of excitatory synapses.[16,22]

The lack of KCC2 recruitment upon extra-synaptic $[K^+]_o$ puff application and the faster, apparently more sensitive astrocytic detection of $[K^+]_o$ (even with low stimulation) compared to ion-sensitive electrodes following synaptic stimulation suggest that the perisynaptic space is a rather separated ECS compartment (similar perisynaptic compartmentalization was reported for glutamate).[45] This view is supported by earlier findings on source-dependent (superfusion vs. synaptic stimulation) discrepancies in effects of $[K^+]_o$ elevations.[9] However, such separation might be overridden as indicated by the nonlinear rise in $[K^+]_o$ recorded by K^+- sensitive electrodes upon synaptic stimulation[9] or the long-known effects of activity-dependent, large-scale $[K^+]_o$ changes.[1]

Regulation of perisynaptic $[K^+]_o$ modulates astrocytic glutamate uptake.[3] Augmented presynaptic glutamate release upon diminished KCC2 activity is intriguing as it supports the proposed mechanism of feedforward K^+ accumulation,[46] i.e., synaptic K^+ release facilitates synaptic activation and, thus, elevation of $[K^+]_o$. Similar augmentation of local excitability of dendrites[47] spreads up to 300 μm after LTP induction. Our study suggests an analogous impact of KCC2 blocking—expanding propensity to excitation to neighboring silent synapses promoting "clustered" plasticity.[48] In other words, KCC2 limits K^+ diffusion to neighboring synapses (that may diffuse easier than the bigger glutamate[49]), thus reducing synchronization but increasing specificity of synaptic inputs—since 88% of nearest neighbors are connected to different presynaptic boutons. In addition, the K^+ again taken by KCC2 into spines could not be re-distributed by astrocytes or contribute to global $[K^+]_o$ changes that influence the cortical state.[50]

Perisynaptic $[K^+]_o$ and therewith synaptic transmission will be influenced by the functional pool of KCC2 that itself is dynamically regulated, most rapidly via multiple posttranslational mechanisms.[12,51] Notably, neuronal activity increases[52] or decreases[44,53] KCC2 expression or activity, depending on different intracellular Ca^{2+} signaling. In addition, KCC2 interacts with a variety of proteins. Whereas some of these regulate KCC2 expression,[54–56] others are regulated by KCC2.[22,23] The latter interaction may lead to (postsynaptic) excitability changes by influencing membrane channels such as TASK-3.[57] Although this interaction did depend on KCC2 expression levels but not on ion flux,[57] and can therefore not directly account for our results, it might boost hyperexcitability resulting from reduced reverse mode if KCC2 expression is chronically reduced.

How can neuronal KCC2-mediated ionic transport in both directions, namely influx and efflux (e.g., in epilepsies), dampen neuronal excitability? While this question currently remains unanswered, a segregation of KCC2 effects in time, state of activity, and space is likely to contribute. The influx we describe here is short, depends on and concerns synaptic excitation, occurs in the vicinity of excitatory synapses (at spines, in which affection of inhibition by $[Cl^-]_i$ changes is less likely), and prevents local $[K^+]_o$ accumulation. The efflux studied by many others is persistent, takes place at dendritic shafts, is triggered by $[Cl^-]_i$ elevations due to (synaptic) inhibition, and keeps $[Cl^-]_i$ low in the long term to ensure inhibition efficiency. Therewith, both effects, $[K^+]_o$ clearance and maintenance of $GABA_A$Rs-mediated hyperpolarization, complement each other to counteract excess excitation and degrade simultaneously when KCC2 is compromised. This should be taken into account when interpreting experimental modulation of KCC2, in situations in which (synaptic) activity alters KCC2 function by changing its membrane presence,[15,44,58] and when considering the contribution of KCC2 to diseases. For example, our findings readily explain the restoration of NMDAR activity upon KCC2 elevation in neuropathic pain.[59] They add another level of complexity to the role of KCC2 (at spines) in epileptic seizures: a temporal KCC2 reversal supports the controversial seizure-protecting role of KCC2,[24] in particular, when other K^+ clearance mechanisms are compromised (e.g., disrupted astrocytic syncytium[60]). Thus, a temporal clearing of elevated perisynaptic $[K^+]_o$ levels adds to the therapeutic potential of KCC2 modulation for various diseases,[61,62] including seizures,[63,64] neuropathic pain,[59,65] and spreading depression.[66]

Limitations of the study

None of our approaches directly recorded perisynaptic $[K^+]_o$; i.e., electrophysiological means cannot provide precise absolute values of $[K^+]_o$ or its changes in the vicinity of a synapse, yet. For technical and anatomical reasons, the currents and voltages we recorded were delayed and attenuated, particularly when we used K^+-selective electrodes. The latter only enable averaged measurements in a restricted space of less than 10 μm and can't be positioned directly at a synapse due to lack of visual control and the putative "shield" by astrocytic endfeet. This matters because we argued previously that $[K^+]_o$ rapidly drops with the distance from synapses.[2] The small and delayed increase in $[K^+]_o$ as detected by K^+-selective electrodes may therefore be read as propagated from a perisynaptic peak.

Astrocytic I_{Kir} recordings appear better suited to capture restricted perisynaptic $[K^+]_o$ fluctuations because astrocytic leaflets are K_{ir} channel rich in regions directly facing the synaptic

cleft and provide a certain separation of the perisynaptic space from the remaining ECS. However, such recordings might still underestimate the role of KCC2 in perisynaptic $[K^+]_o$ uptake, because astrocytic I_{Kir} represents just one of several K^+ uptake mechanisms. Our model reveals that, depending on the strength of stimulation and time after the stimulus, the NA/K-ATPase substantially contributes to the uptake (Figure 3B). Such and alike mechanisms might be even more evident in the biological system. The pronounced Na/K-ATPase contribution upon low stimuli might mask the effect of KCC2 modulation in our I_{Kir} recordings. This prevents us from eventually distinguishing the sensitivity of the method from the assumed insufficiency of a single stimulus to accumulate $[K^+]_o$ that is sufficient for KCC2 reverse mode and therewith from defining an exact threshold stimulus for the KCC2 reverse mode.

Our data suggest that simultaneous $[K^+]_o$ increase in most synapses within the respective astrocytic domain (as achieved by electrical stimulation) and intact fine structure (colocation of pre- and post-synapse, close interactions of astrocytic endfeet with neuronal membranes, narrow and tortuous extracellular matrix) are prerequisites for detecting the reverse mode of KCC2 by astrocytic I_{Kir}. We assume that these prerequisites might not entirely be met by local extracellular pressure injection due to (1) inherent problems of puffing such as mechanical damage, increasing ECS volume, breaking the fragile interactions of tripartite synapse elements, and divergence of consecutive puffs or (2) divergent contribution of other uptake mechanisms (see above) at non-synaptic sites that may limit $[K^+]_o$ or I_{Kir} share in uptake, therewith disabling or masking KCC2 reverse mode. However, such assumptions are speculative, and it remains puzzling why KCC2 inhibition does not affect astrocytic I_{Kir} elicited by K^+ pressure injection.

Having said that the precision of all quantities given is determined by the methods used, this study is rather a proof of concept than comprehensive representation of perisynaptic physiology. This might especially be true for our *in silico* model. As we did not have access to the microscopic single spine parameters, we utilized a simplified lumped model that focuses on capturing the most significant aspects (including the two most prominent uptake mechanisms) of our experiment. Therefore, our model may not encompass all intricacies of the system.

In addition, our experiments cannot unravel the precise origin of $[K^+]_o$, i.e., whether it is NMDA/AMPA[2] or small conductance Ca^{2+}-activated K^+ (SK) channels,[18] but this limitation does not directly concern the conclusions of our study.

In summary, we found a reverse mode of spine KCC2 that provides temporal clearance of perisynaptically elevated $[K^+]_o$ at excitatory synapses. This view reinforces the role of KCC2 as game changer in the excitation-inhibition balance not only during maturation but also in the adult brain, affecting fundamental processes such as presynaptic release, LTP, and spillover. Our findings emphasize the necessity of further studies that explore KCC2-based treatment options.[67]

STAR★METHODS

Detailed methods are provided in the online version of this paper and include the following:

SUPPLEMENTAL INFORMATION

Supplemental information can be found online at https://doi.org/10.1016/j.celrep.2023.112934.

ACKNOWLEDGMENTS

We thank Vladislav V. Shcheslavskiy and Artem Mozherov for supporting the FLIM measurements and Richard Kovacs for help with the potassium-sensitive microelectrodes. This project has received funding from the European Research Council (ERC) under the Union's Horizon 2020 research an innovation program (grant agreement no. 864243) and from the Einstein Foundation Berlin (EP-2021-621). E.B. received a grant of the Ministry of Science and Higher Education of the Russian Federation Academic Excellence Program "priority-2030" from 2017 to 2021.

AUTHOR CONTRIBUTIONS

Conceptualization, E.B., MB., U.S., J.-H.S., S.S., and A.S.; investigation: wet recordings, E.B.; mathematical modeling, M.B.; formal analysis, E.B. and M.B.; supervision, U.S., J.-H.S., T.G., and S.S.; visualization, E.B., T.G., and M.B.; writing – original draft, E.B., U.S., M.B., J.-H.S., and S.S.; writing – review & editing, U.S., S.S., T.G., and A.S.

DECLARATION OF INTERESTS

The authors declare no competing interests.

Received: May 21, 2023
Revised: July 9, 2023
Accepted: July 18, 2023
Published: August 1, 2023

REFERENCES

1. Somjen, G.G. (1979). Extracellular Potassium in the Mammalian Central Nervous System. Annu. Rev. Physiol. *41*, 159–177. https://doi.org/10.1146/annurev.ph.41.030179.001111.
2. Shih, P.-Y., Savtchenko, L.P., Kamasawa, N., Dembitskaya, Y., McHugh, T.J., Rusakov, D.A., Shigemoto, R., and Semyanov, A. (2013). Retrograde synaptic signaling mediated by K+ efflux through postsynaptic NMDA receptors. Cell Rep. *5*, 941–951. https://doi.org/10.1016/j.celrep.2013.10.026.
3. Tyurikova, O., Shih, P.Y., Dembitskaya, Y., Savtchenko, L.P., McHugh, T.J., Rusakov, D.A., and Semyanov, A. (2022). K+ efflux through postsynaptic NMDA receptors suppresses local astrocytic glutamate uptake. Glia *70*, 961–974. https://doi.org/10.1002/glia.24150.

4. Loh, K.H., Stawski, P.S., Draycott, A.S., Udeshi, N.D., Lehrman, E.K., Wilton, D.K., Svinkina, T., Deerinck, T.J., Ellisman, M.H., Stevens, B., et al. (2016). Proteomic Analysis of Unbounded Cellular Compartments: Synaptic Clefts. Cell *166*, 1295–1307.e21. https://doi.org/10.1016/j.cell.2016.07.041.

5. Saghyan, A., Lewis, D.P., Hrabe, J., and Hrabětová, S. (2012). Extracellular diffusion in laminar brain structures exemplified by hippocampus. J. Neurosci. Methods *205*, 110–118. https://doi.org/10.1016/j.jneumeth.2011.12.008.

6. Syková, E., and Nicholson, C. (2008). Diffusion in brain extracellular space. Physiol. Rev. *88*, 1277–1340. https://doi.org/10.1152/physrev.00027.2007.

7. Kofuji, P., and Newman, E.A. (2004). Potassium buffering in the central nervous system. Neuroscience *129*, 1045–1056. https://doi.org/10.1016/j.neuroscience.2004.06.008.

8. Pérez-Pinzón, M.A., Tao, L., and Nicholson, C. (1995). Extracellular potassium, volume fraction, and tortuosity in rat hippocampal CA1, CA3, and cortical slices during ischemia. J. Neurophysiol. *74*, 565–573. https://doi.org/10.1152/jn.1995.74.2.565.

9. Poolos, N.P., Mauk, M.D., and Kocsis, J.D. (1987). Activity-evoked increases in extracellular potassium modulate presynaptic excitability in the CA1 region of the hippocampus. J. Neurophysiol. *58*, 404–416. https://doi.org/10.1152/jn.1987.58.2.404.

10. Rivera, C., Voipio, J., Payne, J.A., Ruusuvuori, E., Lahtinen, H., Lamsa, K., Pirvola, U., Saarma, M., and Kaila, K. (1999). The K+/Cl- co-transporter KCC2 renders GABA hyperpolarizing during neuronal maturation. Nature *397*, 251–255. https://doi.org/10.1038/16697.

11. Chamma, I., Chevy, Q., Poncer, J.-C., and Lévi, S. (2012). Role of the neuronal K-Cl co-transporter KCC2 in inhibitory and excitatory neurotransmission. Front. Cell. Neurosci. *6*, 5. https://doi.org/10.3389/fncel.2012.00005.

12. Côme, E., Marques, X., Poncer, J.-C., and Lévi, S. (2019). KCC2 membrane diffusion tunes neuronal chloride homeostasis. Neuropharmacology107571. https://doi.org/10.1016/j.neuropharm.2019.03.014.

13. Ferando, I., Faas, G.C., and Mody, I. (2016). Diminished KCC2 confounds synapse specificity of LTP during senescence. Nat. Neurosci. *19*, 1197–1200. https://doi.org/10.1038/nn.4357.

14. Gulyás, A.I., Sík, A., Payne, J.A., Kaila, K., and Freund, T.F. (2001). The KCl cotransporter, KCC2, is highly expressed in the vicinity of excitatory synapses in the rat hippocampus. Eur. J. Neurosci. *13*, 2205–2217.

15. Heubl, M., Zhang, J., Pressey, J.C., Al Awabdh, S., Renner, M., Gomez-Castro, F., Moutkine, I., Eugène, E., Russeau, M., Kahle, K.T., et al. (2017). GABAA receptor dependent synaptic inhibition rapidly tunes KCC2 activity via the Cl–sensitive WNK1 kinase. Nat. Commun. *8*, 1776. https://doi.org/10.1038/s41467-017-01749-0.

16. Gauvain, G., Chamma, I., Chevy, Q., Cabezas, C., Irinopoulou, T., Bodrug, N., Carnaud, M., Lévi, S., and Poncer, J.-C. (2011). The neuronal K-Cl cotransporter KCC2 influences postsynaptic AMPA receptor content and lateral diffusion in dendritic spines. Proc. Natl. Acad. Sci. USA *108*, 15474–15479. https://doi.org/10.1073/pnas.1107893108.

17. Báldi, R., Varga, C., and Tamás, G. (2010). Differential distribution of KCC2 along the axo-somato-dendritic axis of hippocampal principal cells. Eur. J. Neurosci. *32*, 1319–1325. https://doi.org/10.1111/j.1460-9568.2010.07361.x.

18. Weilinger, N.L., Wicki-Stordeur, L.E., Groten, C.J., LeDue, J.M., Kahle, K.T., and MacVicar, B.A. (2022). KCC2 drives chloride microdomain formation in dendritic blebbing. Cell Rep. *41*, 111556. https://doi.org/10.1016/j.celrep.2022.111556.

19. Awad, P.N., Amegandjin, C.A., Szczurkowska, J., Carriço, J.N., Fernandes do Nascimento, A.S., Baho, E., Chattopadhyaya, B., Cancedda, L., Carmant, L., and Di Cristo, G. (2018). KCC2 Regulates Dendritic Spine Formation in a Brain-Region Specific and BDNF Dependent Manner. Cerebr. Cortex *28*, 4049–4062. https://doi.org/10.1093/cercor/bhy198.

20. Fiumelli, H., Briner, A., Puskarjov, M., Blaesse, P., Belem, B.J., Dayer, A.G., Kaila, K., Martin, J.-L., and Vutskits, L. (2013). An Ion Transport-independent Role for the Cation-Chloride Cotransporter KCC2 in Dendritic Spinogenesis in Vivo, *23* (Cerebral cortex), pp. 378–388. https://doi.org/10.1093/cercor/bhs027.

21. Li, H., Khirug, S., Cai, C., Ludwig, A., Blaesse, P., Kolikova, J., Afzalov, R., Coleman, S.K., Lauri, S., Airaksinen, M.S., et al. (2007). KCC2 interacts with the dendritic cytoskeleton to promote spine development. Neuron *56*, 1019–1033. https://doi.org/10.1016/j.neuron.2007.10.039.

22. Chevy, Q., Heubl, M., Goutierre, M., Backer, S., Moutkine, I., Eugène, E., Bloch-Gallego, E., Lévi, S., and Poncer, J.C. (2015). KCC2 Gates Activity-Driven AMPA Receptor Traffic through Cofilin Phosphorylation. J. Neurosci. *35*, 15772–15786. https://doi.org/10.1523/jneurosci.1735-15.2015.

23. Llano, O., Smirnov, S., Soni, S., Golubtsov, A., Guillemin, I., Hotulainen, P., Medina, I., Nothwang, H.G., Rivera, C., and Ludwig, A. (2015). KCC2 regulates actin dynamics in dendritic spines via interaction with β-PIX. J. Cell Biol. *209*, 671–686. https://doi.org/10.1083/jcb.201411008.

24. Kaila, K., Price, T.J., Payne, J.A., Puskarjov, M., and Voipio, J. (2014). Cation-chloride cotransporters in neuronal development, plasticity and disease. Nat. Rev. Neurosci. *15*, 637–654. https://doi.org/10.1038/nrn3819.

25. DeFazio, R.A., Keros, S., Quick, M.W., and Hablitz, J.J. (2000). Potassium-coupled chloride cotransport controls intracellular chloride in rat neocortical pyramidal neurons. J. Neurosci. *20*, 8069–8076. https://doi.org/10.1523/jneurosci.20-21-08069.2000.

26. Payne, J.A. (1997). Functional characterization of the neuronal-specific K-Cl cotransporter: implications for [K+]o regulation. Am. J. Physiol. *273*. C1516-C1525.

27. Düsterwald, K.M., Currin, C.B., Burman, R.J., Akerman, C.J., Kay, A.R., and Raimondo, J.V. (2018). Biophysical models reveal the relative importance of transporter proteins and impermeant anions in chloride homeostasis. Elife *7*, 302. https://doi.org/10.7554/elife.39575.

28. Jarolimek, W., Lewen, A., and Misgeld, U. (1999). A furosemide-sensitive K+-Cl- cotransporter counteracts intracellular Cl- accumulation and depletion in cultured rat midbrain neurons. J. Neurosci. *19*, 4695–4704. https://doi.org/10.1523/jneurosci.19-12-04695.1999.

29. Kakazu, Y., Uchida, S., Nakagawa, T., Akaike, N., and Nabekura, J. (2000). Reversibility and cation selectivity of the K(+)-Cl(-) cotransport in rat central neurons. J. Neurophysiol. *84*, 281–288. https://doi.org/10.1152/jn.2000.84.1.281.

30. Henneberger, C., Bard, L., Panatier, A., Reynolds, J.P., Kopach, O., Medvedev, N.I., Minge, D., Herde, M.K., Anders, S., Kraev, I., et al. (2020). LTP Induction Boosts Glutamate Spillover by Driving Withdrawal of Perisynaptic Astroglia. Neuron *108*, 919–936.e11. https://doi.org/10.1016/j.neuron.2020.08.030.

31. Rose, C.R., and Konnerth, A. (2001). NMDA Receptor-Mediated Na+ Signals in Spines and Dendrites. J. Neurosci. *21*, 4207–4214. https://doi.org/10.1523/jneurosci.21-12-04207.2001.

32. Larsen, B.R., Assentoft, M., Cotrina, M.L., Hua, S.Z., Nedergaard, M., Kaila, K., Voipio, J., and MacAulay, N. (2014). Contributions of the Na^+/K^+-ATPase, NKCC1, and Kir4.1 to hippocampal K^+ clearance and volume responses. Glia *62*, 608–622. https://doi.org/10.1002/glia.22629.

33. Olsen, M.L., Higashimori, H., Campbell, S.L., Hablitz, J.J., and Sontheimer, H. (2006). Functional expression of Kir4.1 channels in spinal cord astrocytes. Glia *53*, 516–528. https://doi.org/10.1002/glia.20312.

34. Sibille, J., Pannasch, U., and Rouach, N. (2014). Astroglial potassium clearance contributes to short-term plasticity of synaptically evoked currents at the tripartite synapse. J. Physiol. *592*, 87–102. https://doi.org/10.1113/jphysiol.2013.261735.

35. Cardarelli, R.A., Jones, K., Pisella, L.I., Wobst, H.J., McWilliams, L.J., Sharpe, P.M., Burnham, M.P., Baker, D.J., Chudotvorova, I., Guyot, J., et al. (2017). The small molecule CLP257 does not modify activity of the

K+-Cl- co-transporter KCC2 but does potentiate GABAA receptor activity. Nat. Med. *23*, 1394–1396. https://doi.org/10.1038/nm.4442.

36. Ghézali, G., Vasile, F., Curry, N., Fantham, M., Cheung, G., Ezan, P., Cohen-Salmon, M., Kaminski, C., and Rouach, N. (2020). Neuronal Activity Drives Astroglial Connexin 30 in Perisynaptic Processes and Shapes its Functions, *30* (Cerebral cortex), pp. 753–766. https://doi.org/10.1093/cercor/bhz123.
37. Wallraff, A., Köhling, R., Heinemann, U., Theis, M., Willecke, K., and Steinhäuser, C. (2006). The impact of astrocytic gap junctional coupling on potassium buffering in the hippocampus. J. Neurosci. *26*, 5438–5447. https://doi.org/10.1523/jneurosci.0037-06.2006.
38. Rusakov, D.A., Harrison, E., and Stewart, M.G. (1998). Synapses in hippocampus occupy only 1-2% of cell membranes and are spaced less than half-micron apart: a quantitative ultrastructural analysis with discussion of physiological implications. Neuropharmacology *37*, 513–521. https://doi.org/10.1016/s0028-3908(98)00023-9.
39. Semyanov, A., and Verkhratsky, A. (2021). Astrocytic processes: from tripartite synapses to the active milieu. Trends Neurosci. *44*, 781–792. https://doi.org/10.1016/j.tins.2021.07.006.
40. Popov, A., Denisov, P., Bychkov, M., Brazhe, A., Lyukmanova, E., Shenkarev, Z., Lazareva, N., Verkhratsky, A., and Semyanov, A. (2020). Caloric restriction triggers morphofunctional remodeling of astrocytes and enhances synaptic plasticity in the mouse hippocampus. Cell Death Dis. *11*, 208. https://doi.org/10.1038/s41419-020-2406-3.
41. Popov, A., Brazhe, A., Denisov, P., Sutyagina, O., Li, L., Lazareva, N., Verkhratsky, A., and Semyanov, A. (2021). Astrocyte dystrophy in ageing brain parallels impaired synaptic plasticity. Aging Cell *20*, e13334. https://doi.org/10.1111/acel.13334.
42. Plata, A., Lebedeva, A., Denisov, P., Nosova, O., Postnikova, T.Y., Pimashkin, A., Brazhe, A., Zaitsev, A.V., Rusakov, D.A., and Semyanov, A. (2018). Astrocytic Atrophy Following Status Epilepticus Parallels Reduced Ca2+ Activity and Impaired Synaptic Plasticity in the Rat Hippocampus. Front. Mol. Neurosci. *11*, 215. https://doi.org/10.3389/fnmol.2018.00215.
43. Dzhala, V., Valeeva, G., Glykys, J., Khazipov, R., and Staley, K. (2012). Traumatic alterations in GABA signaling disrupt hippocampal network activity in the developing brain. J. Neurosci. *32*, 4017–4031. https://doi.org/10.1523/jneurosci.5139-11.2012.
44. Chamma, I., Heubl, M., Chevy, Q., Renner, M., Moutkine, I., Eugène, E., Poncer, J.-C., and Lévi, S. (2013). Activity-dependent regulation of the K/Cl transporter KCC2 membrane diffusion, clustering, and function in hippocampal neurons. J. Neurosci. *33*, 15488–15503. https://doi.org/10.1523/jneurosci.5889-12.2013.
45. Wu, Y.-W., Grebenyuk, S., McHugh, T.J., Rusakov, D.A., and Semyanov, A. (2012). Backpropagating action potentials enable detection of extrasynaptic glutamate by NMDA receptors. Cell Rep. *1*, 495–505. https://doi.org/10.1016/j.celrep.2012.03.007.
46. GRAFSTEIN, B. (1956). Mechanism of spreading cortical depression. J. Neurophysiol. *19*, 154–171. https://doi.org/10.1152/jn.1956.19.2.154.
47. Frick, A., Magee, J., and Johnston, D. (2004). LTP is accompanied by an enhanced local excitability of pyramidal neuron dendrites. Nat. Neurosci. *7*, 126–135. https://doi.org/10.1038/nn1178.
48. Harvey, C.D., and Svoboda, K. (2007). Locally dynamic synaptic learning rules in pyramidal neuron dendrites. Nature *450*, 1195–1200. https://doi.org/10.1038/nature06416.
49. Malenka, R.C., and Nicoll, R.A. (1997). Silent synapses speak up. Neuron *19*, 473–476. https://doi.org/10.1016/s0896-6273(00)80362-1.
50. Rasmussen, R., Nicholas, E., Petersen, N.C., Dietz, A.G., Xu, Q., Sun, Q., and Nedergaard, M. (2019). Cortex-wide Changes in Extracellular Potassium Ions Parallel Brain State Transitions in Awake Behaving Mice. Cell Rep. *28*, 1182–1194.e4. https://doi.org/10.1016/j.celrep.2019.06.082.
51. Medina, I., Friedel, P., Rivera, C., Kahle, K.T., Kourdougli, N., Uvarov, P., and Pellegrino, C. (2014). Current view on the functional regulation of the neuronal K(+)-Cl(-) cotransporter KCC2. Front. Cell. Neurosci. *8*, 27. https://doi.org/10.3389/fncel.2014.00027.
52. Chorin, E., Vinograd, O., Fleidervish, I., Gilad, D., Herrmann, S., Sekler, I., Aizenman, E., and Hershfinkel, M. (2011). Upregulation of KCC2 Activity by Zinc-Mediated Neurotransmission via the mZnR/GPR39 Receptor. J. Neurosci. *31*, 12916–12926. https://doi.org/10.1523/jneurosci.2205-11.2011.
53. Fiumelli, H., Cancedda, L., and Poo, M.m. (2005). Modulation of GABAergic Transmission by Activity via Postsynaptic Ca2+-Dependent Regulation of KCC2 Function. Neuron *48*, 773–786. https://doi.org/10.1016/j.neuron.2005.10.025.
54. Ivakine, E.A., Acton, B.A., Mahadevan, V., Ormond, J., Tang, M., Pressey, J.C., Huang, M.Y., Ng, D., Delpire, E., Salter, M.W., et al. (2013). Neto2 is a KCC2 interacting protein required for neuronal Cl− regulation in hippocampal neurons. Proc. Natl. Acad. Sci. USA *110*, 3561–3566. https://doi.org/10.1073/pnas.1212907110.
55. Mahadevan, V., and Woodin, M.A. (2016). Regulation of neuronal chloride homeostasis by neuromodulators. J. Physiol. *594*, 2593–2605. https://doi.org/10.1113/jp271593.
56. Wright, R., Newey, S.E., Ilie, A., Wefelmeyer, W., Raimondo, J.V., Ginham, R., McIlhinney, R.A.J., and Akerman, C.J. (2017). Neuronal Chloride Regulation via KCC2 Is Modulated through a GABAB Receptor Protein Complex. J. Neurosci. *37*, 5447–5462. https://doi.org/10.1523/jneurosci.2164-16.2017.
57. Goutierre, M., Al Awabdh, S., Donneger, F., François, E., Gomez-Dominguez, D., Irinopoulou, T., Menendez de la Prida, L., and Poncer, J.-C. (2019). KCC2 Regulates Neuronal Excitability and Hippocampal Activity via Interaction with Task-3 Channels. Cell Rep. *28*, 91–103.e7. https://doi.org/10.1016/j.celrep.2019.06.001.
58. Côme, E., Heubl, M., Schwartz, E.J., Poncer, J.-C., and Lévi, S. (2019). Reciprocal Regulation of KCC2 Trafficking and Synaptic Activity. Front. Cell. Neurosci. *13*, 48. https://doi.org/10.3389/fncel.2019.00048.
59. Li, L., Chen, S.-R., Chen, H., Wen, L., Hittelman, W.N., Xie, J.-D., and Pan, H.-L. (2016). Chloride Homeostasis Critically Regulates Synaptic NMDA Receptor Activity in Neuropathic Pain. Cell Rep. *15*, 1376–1383. https://doi.org/10.1016/j.celrep.2016.04.039.
60. Nakase, T., and Naus, C.C.G. (2004). Gap junctions and neurological disorders of the central nervous system. Biochim. Biophys. Acta *1662*, 149–158. https://doi.org/10.1016/j.bbamem.2004.01.009.
61. Hyde, T.M., Lipska, B.K., Ali, T., Mathew, S.V., Law, A.J., Metitiri, O.E., Straub, R.E., Ye, T., Colantuoni, C., Herman, M.M., et al. (2011). Expression of GABA signaling molecules KCC2, NKCC1, and GAD1 in cortical development and schizophrenia. J. Neurosci. *31*, 11088–11095. https://doi.org/10.1523/jneurosci.1234-11.2011.
62. Kahle, K.T., Staley, K.J., Nahed, B.V., Gamba, G., Hebert, S.C., Lifton, R.P., and Mount, D.B. (2008). Roles of the cation-chloride cotransporters in neurological disease. Nature clinical practice. Neurology *4*, 490–503. https://doi.org/10.1038/ncpneuro0883.
63. Magloire, V., Cornford, J., Lieb, A., Kullmann, D.M., and Pavlov, I. (2019). KCC2 overexpression prevents the paradoxical seizure-promoting action of somatic inhibition. Nat. Commun. *10*, 1225. https://doi.org/10.1038/s41467-019-08933-4.
64. Moore, Y.E., Kelley, M.R., Brandon, N.J., Deeb, T.Z., and Moss, S.J. (2017). Seizing Control of KCC2: A New Therapeutic Target for Epilepsy. Trends Neurosci. *40*, 555–571. https://doi.org/10.1016/j.tins.2017.06.008.
65. Mapplebeck, J.C.S., Lorenzo, L.-E., Lee, K.Y., Gauthier, C., Muley, M.M., De Koninck, Y., Prescott, S.A., and Salter, M.W. (2019). Chloride Dysregulation through Downregulation of KCC2 Mediates Neuropathic Pain in Both Sexes. Cell Rep. *28*, 590–596.e4. https://doi.org/10.1016/j.celrep.2019.06.059.
66. Desroches, M., Faugeras, O., Krupa, M., and Mantegazza, M. (2019). Modeling cortical spreading depression induced by the hyperactivity of

interneurons. J. Comput. Neurosci. *47*, 125–140. https://doi.org/10.1007/s10827-019-00730-8.

67. Tang, B.L. (2020). The Expanding Therapeutic Potential of Neuronal KCC2. Cells *9*. https://doi.org/10.3390/cells9010240.
68. Arizono, M., Inavalli, V.V.G.K., Panatier, A., Pfeiffer, T., Angibaud, J., Levet, F., Ter Veer, M.J.T., Stobart, J., Bellocchio, L., Mikoshiba, K., et al. (2020). Structural basis of astrocytic Ca2+ signals at tripartite synapses. Nat. Commun. *11*, 1906–1915. https://doi.org/10.1038/s41467-020-15648-4.
69. Dallérac, G., Chever, O., and Rouach, N. (2013). How do astrocytes shape synaptic transmission? Insights from electrophysiology. Front. Cell. Neurosci. *7*, 159. https://doi.org/10.3389/fncel.2013.00159.
70. Delpire, E., Baranczak, A., Waterson, A.G., Kim, K., Kett, N., Morrison, R.D., Daniels, J.S., Weaver, C.D., and Lindsley, C.W. (2012). Further optimization of the K-Cl cotransporter KCC2 antagonist ML077: development of a highly selective and more potent in vitro probe. Bioorg. Med. Chem. Lett. *22*, 4532–4535. https://doi.org/10.1016/j.bmcl.2012.05.126.
71. Sivakumaran, S., Cardarelli, R.A., Maguire, J., Kelley, M.R., Silayeva, L., Morrow, D.H., Mukherjee, J., Moore, Y.E., Mather, R.J., Duggan, M.E., et al. (2015). Selective inhibition of KCC2 leads to hyperexcitability and epileptiform discharges in hippocampal slices and in vivo. J. Neurosci. *35*, 8291–8296. https://doi.org/10.1523/jneurosci.5205-14.2015.
72. Spoljaric, I., Spoljaric, A., Mavrovic, M., Seja, P., Puskarjov, M., and Kaila, K. (2019). KCC2-Mediated Cl- Extrusion Modulates Spontaneous Hippocampal Network Events in Perinatal Rats and Mice. Cell Rep. *26*, 1073–1081.e3. https://doi.org/10.1016/j.celrep.2019.01.011.
73. Witthoft, A., Filosa, J.A., and Karniadakis, G.E. (2013). Potassium buffering in the neurovascular unit: models and sensitivity analysis. Biophys. J. *105*, 2046–2054. https://doi.org/10.1016/j.bpj.2013.09.012.
74. Barreto, E., and Cressman, J.R. (2011). Ion concentration dynamics as a mechanism for neuronal bursting. J. Biol. Phys. *37*, 361–373. https://doi.org/10.1007/s10867-010-9212-6.
75. Park, E.-H., and Durand, D.M. (2006). Role of potassium lateral diffusion in non-synaptic epilepsy: a computational study. J. Theor. Biol. *238*, 666–682. https://doi.org/10.1016/j.jtbi.2005.06.015.
76. Bushong, E.A., Martone, M.E., Jones, Y.Z., and Ellisman, M.H. (2002). Protoplasmic astrocytes in CA1 stratum radiatum occupy separate anatomical domains. J. Neurosci. *22*, 183–192. https://doi.org/10.1523/jneurosci.22-01-00183.2002.
77. Kirov, S.A., Sorra, K.E., and Harris, K.M. (1999). Slices have more synapses than perfusion-fixed hippocampus from both young and mature rats. J. Neurosci. *19*, 2876–2886.
78. Savtchenko, L.P., and Rusakov, D.A. (2007). The optimal height of the synaptic cleft. Proc. Natl. Acad. Sci. USA *104*, 1823–1828. https://doi.org/10.1073/pnas.0606636104.
79. Octeau, J.C., Chai, H., Jiang, R., Bonanno, S.L., Martin, K.C., and Khakh, B.S. (2018). An Optical Neuron-Astrocyte Proximity Assay at Synaptic Distance Scales. Neuron *98*, 49–66.e9. https://doi.org/10.1016/j.neuron.2018.03.003.
80. Thorne, R.G., and Nicholson, C. (2006). In vivo diffusion analysis with quantum dots and dextrans predicts the width of brain extracellular space. Proc. Natl. Acad. Sci. USA *103*, 5567–5572. https://doi.org/10.1073/pnas.0509425103.
81. Harris, K.M., and Stevens, J.K. (1989). Dendritic spines of CA 1 pyramidal cells in the rat hippocampus: serial electron microscopy with reference to their biophysical characteristics. J. Neurosci. *9*, 2982–2997. https://doi.org/10.1523/jneurosci.09-08-02982.1989.

STAR★METHODS

KEY RESOURCES TABLE

REAGENT or RESOURCE	SOURCE	IDENTIFIER
Chemicals, peptides, and recombinant proteins		
(−)-Bicuculline methiodide	Tocris, Bristol, UK	CAS 40709-69-1
VU0463271	Tocris, Bristol, UK	CAS 1391737-01-1
CLP257	Tocris, Bristol, UK	CAS 1181081-71-9
Closantel	Sigma-Aldrich, Steinheim, Germany	CAS 57808-65-8
CNQX disodium salt	Tocris, Bristol, UK	CAS 479347-85-8
DAP-5	Tocris, Bristol, UK	CAS 79055-68-8
CGP54626 hydrochloride	Tocris, Bristol, UK	CAS 149184-21-4
Carbenoxolone	Sigma-Aldrich, Steinheim, Germany	CAS 7421-40-1
$BaCl_2$	Sigma-Aldrich, Steinheim, Germany	CAS 10361-37-2
Alexa Fluor 647 Streptavidin	Invitrogen	S-21374
Biocytin	Invitrogen	CAS 576-19-2
MQAE	Sigma-Aldrich, Steinheim, Germany	CAS 162558-52-3
Alexa Fluor 594	Thermo Fisher Scientific, USA	
Experimental Models: Organisms/Strains		
Mouse: C57BL/6J	The Jackson Laboratory	Stock No: 000664
Software and algorithms		
PatchMaster	HEKA, Lambrecht, Germany	https://www.heka.com/
FitMaster	HEKA, Lambrecht, Germany	https://www.heka.com/
Origin 2019	OriginLab Corporation, Northampton, USA	https://www.originlab.com/
Python	Python Software Foundation	https://www.python.org/
The code generated during this study	This paper	https://doi.org/10.5281/zenodo.8146820
Brian2 (open source simulator for spiking neural networks)	Stimberg M, Brette R, Goodman DFM (2019). Brian 2, an intuitive and efficient neural simulator. eLife 8:e47314. https://doi.org/10.7554/eLife.47314	N/A

RESOURCE AVAILABILITY

Lead contact

Further information and requests for resources and reagents should be directed to and will be fulfilled by the Lead Contact, Ulf Strauss (ulf.strauss@charite.de).

Materials availability

This study did not generate new unique reagents.

Data and code availability

- All data reported in this paper will be shared by the lead contact upon request.
- All original code has been deposited at Zenodo and is publicly available as of the date of publication. DOI is listed in the key resources table.
- Any additional information required to reanalyze the data reported in this paper is available from the lead contact upon request.

EXPERIMENTAL MODEL AND SUBJECT DETAILS

Experimental animals

C57BL/6J 4–5 weeks old male mice were used for experiments. All animals were kept at 12h day/night cycle at Charité central animal facility FEM (Berlin, Germany) with free access to water and food. All procedures were performed in agreement with the European

Communities Council Directive of September 22, 2010 (2010/63/EU) and carried out in accordance with state of Berlin rules (registration no. T0212/14).

METHOD DETAILS

Slice preparation

Mice were deeply anesthetized with isofluorane and brain blocks containing hippocampus removed. Coronal slices 300 μm thick were cut on a Leica VT1000S vibratome in cold (2°C) solution containing (in mM): 85 NaCl, 2.5 KCl, 0.5 $CaCl_2$, 26 $NaHCO_3$, 1 NaH_2PO_4, 7 $MgCl_2$, 50 sucrose and 10 glucose, pH 7.4. Slices recovered for 30 min in the same solution at 34°C and then maintained in modified solution containing (in mM): 92 NaCl, 30 $NaHCO_3$, 2.5 KCl, 2 $MgSO_4$, 2 $CaCl_2$, 1.2 NaH2PO4, 2 thiourea, 3 Na-pyruvate, 5 Na-ascorbate and 10 glucose, pH 7.4 at room temperature (21°C–23°C). For experiments, slices were transferred to a submerged recording chamber mounted on an Olympus BX51WI microscope equipped for infra-red differential interference contrast microscopy and perfused with artificial cerebrospinal fluid (ACSF) at 34 °C at a rate of 2 mL min^{-1}. ACSF contained (in mM): 119 NaCl, 2.5 KCl, 2.5 $CaCl_2$, 26 $NaHCO_3$, 1 NaH_2PO_4, 1.3 $MgCl_2$ and 10 glucose, pH 7.4. All solutions were bubbled with 95% O_2/5% CO_2.

Electrophysiology

Extracellular bipolar tungsten stimulating electrode was placed in CA1 *str. radiatum* field of hippocampal slice. Each stimulation pulse had rectangular shape and the duration of 200 μsec. Field excitatory postsynaptic potentials (fEPSPs) were recorded in CA1 *s. radiatum* using glass pipettes with resistance of 1–2 MΩ filled with ACSF. Infrared differential interference contrast microscopy was used for visual identification of astrocytes of CA1 *s. radiatum* and neurons in CA1 *s. pyramidale*. Cells 30–70 μm from slice surface and at least 250 μm from the stimulating electrode were used for experiments. Pipettes for somatic whole-cell patch experiments on pyramidal neurons (3–6 MΩ) contained (in mM): 128 potassium gluconate, 2 KCl, 11 EGTA, 10 HEPES, 10 Na-phosphocreatine, 2 Mg-ATP, 0.3 GTP, 1 $MgCl_2$ and 1 $CaCl_2$ (pH 7.2, 300 mosmol l^{-1}). Pipettes for somatic whole-cell patch experiments of astrocytes had resistance of 3–6 MΩ when filled with (in mM): 105 potassium gluconate, 30 KCl, 10 HEPES, 10 Na-phosphocreatine, 4 MgATP, 0.3 Na-GTP and 0.3 EGTA (pH 7.3, 280 mosmol l^{-1}). Astrocytes were identified by small soma (5–10 μm), resting membrane potentials around −80 mV, low membrane resistance (6–15 MΩ) and passive membrane properties (linear I–V relation, Figure 1A, inset). Recordings were started at least 5 min after obtaining whole cell configuration to allow intracellular solution to equilibrate. Astrocytes provide a physiological measure of $[K^+]_o$ gradients and dynamics. Whole-cell patch-clamp recordings at the astrocyte soma do not alter perisynaptic tissue structure. Astrocytic spongiform domains infiltrate the entire neuropil and contact 90% of spines closely and stably.[68] Their inward rectifying K^+ channels (K_{ir})[7] render them highly sensitive to $[K^+]_o$ changes during synaptic transmission.[34,69] Notably, KCC2 is not expressed in astroglia which restricts pharmacological effects to neuron specific KCC2. Astrocytic K_{ir} currents (I_{Kir}) can, therefore, be assumed to correlate with neuronal KCC2 potassium flux. Astrocytes were clamped at −80 mV in voltage clamp mode recordings and at 0 pA in current clamp mode and neurons were clamped at −70 mV.

Data was recorded with an EPC-10 USB double amplifier (HEKA, Lambrecht, Germany), digitized with sampling rate minimum of 10 kHz, stored using the PatchMaster software (HEKA) and analyzed using FitMaster (HEKA) and Origin2019 (OriginLab) software. Series or input resistance change of 20% or less was tolerated during experiment otherwise result was excluded from statistical analysis.

Morphology

In some experiments, astrocytes were filled with biocytin (0.1%, Invitrogen) and stained *post hoc*. In brief, slices were kept in 4% paraformaldehyde in 0.1% phosphate buffer (PB) (pH = 7.4) at room temperature for 1 h and then transferred to 0.1% PB at 4°C. Prior to visualization, slices were washed 5 times in PB and incubated with fluorescent-conjugated streptavidin (Alexa Fluor 647, 1:1000, Invitrogen), in a PBS solution containing 3% normal goat serum, 0.1% Triton X-100, and 0.05% NaN_3 for 48 h at 4°C. After incubation slices were washed in PB 5 times and mounted onto glass coverslips for further visualization. Counterstained astrocytes were imaged and identified using laser scanning confocal microscopy.

Fluorescence lifetime imaging microscopy (FLIM)

Experiments have been performed using confocal one-photon and two-photon laser scanning microscope LSM 880 (Carl Zeiss, Jena, Germany) equipped with fs Ti:sapphire laser (Mai Tai HP (Spectra Physics, Milipitas, Ca, USA) operating at 80 MHz repetition rate. Average power incident on a sample was 5 mW. Prior to visualization slices were incubated in ASCF with 5 mM MQAE for 30 min at 34°C. Samples were excited at 750 nm and fluorescence signal was detected from 435 nm to 485 nm using band-pass filter (460/50 BP, Chroma, Vt, US) and short pass filter (690 SP, Chroma, US) with HPM-100-40 GaAsP-hybrid detector (Becker & Hickl GmbH, Berlin, Germany) at NDD-port working in single photon counting mode. Single photon counting card SPC-150 (Becker & Hickl GmbH, Germany) was used to acquire photon statistics, which was further processed in SPCIMAGE 8.5 (Becker & Hickl GmbH, Germany).

Experiment design and reagents

Schaffer collaterals were stimulated with 20 pulses 10 ms apart. To minimize ongoing LTP, 2 preconditioning trains with 5 min interval were applied before proceeding with recordings and control trace was acquired 5 min after 2nd preconditioning train. For less synaptic activity 5 pulses 50 ms apart were used without prior stimulation.

In puffing experiments glass pipet containing (in mM): 91.5 NaCl, 30 KCl, 2.5 $CaCl_2$, 26 $NaHCO_3$, 1 NaH_2PO_4, 1.3 MgCl2 and 10 glucose was positioned 50 μm from soma of patched astrocyte. Puff duration was 200 ms to mimic the K^+ exposure time as with electrical stimulation.

All experiments were performed in presence of a $GABA_A$ antagonist, either (−)-Bicuculline methiodide (Tocris, Bristol, UK) (10 μM) or Picrotoxin (Tocris, Bristol, UK) (100 μM) and a cut was made between CA1 and CA3 to prevent the development of epileptiform activity. KCC2 was blocked with 10 μM VU0463271 (Tocris, Bristol, UK), based on its efficacy/reliability in brain slices[70–72] (dose dependence of VU0463271 approaches 100% at concentrations $> \sim 5$ μM[70]). KCC2 was enhanced with 50 μM CLP257 (Tocris, Bristol, UK) or 10 μM closantel (Sigma-Aldrich, Steinheim, Germany).

Glutamatergic excitatory transmission was blocked with 20 μM CNQX disodium salt (AMPA receptors blocker) (Tocris, Bristol, UK) and 25 μM DAP-5 (NMDA receptors blocker) (Tocris, Bristol, UK). $GABA_B$ receptors were blocked with 10 μM CGP54626 (Tocris, Bristol, UK). K^+ inward rectifying channels were blocked with 200 μM $BaCl_2$ (Sigma-Aldrich, Steinheim, Germany). Gap-junctions of astrocytes were disrupted by 100 μM carbenoxolone (CBX, Sigma-Aldrich, Steinheim, Germany). Perfusion time for VU0463271, CLP257, closantel and CGP54626 was set to $\geq$12 min, for CNQX disodium salt, DAP-5 and $BaCl_2$ to $\geq$5 min, for CBX to $\geq$20 min. In LTP experiments potentiation was induced by Schaffer collateral stimulation train (20 pulses at 100 Hz) without preconditioning.

Mathematical model

The model consists of three compartments: effective spine, perisynaptic extracellular space (pECS), and astrocyte compartment (Figure 3A). The effective spine compartment accounts for all spines related to one astrocytic compartment. The pECS compartment combines all clefts and extracellular matrix that is under influence of both, spine (KCC2 co-transporter, Na/K-ATPase, etc.) and astrocytic K^+ regulation. The extracellular K^+ concentration $[K^+]_o$ changes dynamically according to the mass balance equation:

$$\frac{d[K^+]_o}{dt} = J_{Kir} - J_{KCC2} - J_{Na/K-ATPase} + J_{stimulation} - r_{se}J_{leakage} \quad \text{(Equation 1)}$$

The K^+ flux, J_{kir}, from the pECS compartment to the astrocyte compartment is mediated by the inward rectifying K^+ current (I_{Kir}). The K^+/Cl^--co-transporter KCC2 is responsible for J_{KCC2}. In addition, $J_{Na/K\text{-}ATPase}$ represents the Na/K-ATPase flux of the spine compartment. $J_{stimulation}$ is a 1 s "stimulus" K^+ flux of 10 mM/s or 1 mM/s that enters the pECS from the spine compartment. $J_{leakage}$ is a leakage flux affected by K^+ concentration inside the spine compartment. This flux is multiplied by the volume ratio of the spine to pECS compartments (r_{se}) to get the suitable flux for this equation. Before applying the stimulus, we made sure that in the resting phase of the model, the variables are in the biological range. The main (experimentally accessible) readout for model fitting, is astrocytic I_{Kir} defined by Equation 3, where $Volume_{ex}$ is the pECS volume and F is Faraday's constant.

$$J_{Kir} = \frac{I_{Kir}}{F \times Volume_{ex}} \quad \text{(Equation 2)}$$

I_{Kir} is defined as in[73].

$$I_{Kir} = g_{Kir}\left(V_{astrocyte} - V_{Kir}\right) \quad \text{(Equation 3)}$$

where the Ohmic conductance depends on $[K^+]_o$ in a square-root law

$$g_{Kir} = g_{Kir0}\sqrt{[K^+]_o} \quad \text{(Equation 4)}$$

The astrocyte is clamped to a potential of $V_{astrocyte} = -80$ mV, as in the experiments. The reversal potential for I_{Kir} is given by the Nernst equation

$$V_{Kir} = \frac{RT}{Fz}\ln\left(\frac{[K^+]_o}{[K^+]_{astrocyte}}\right) \quad \text{(Equtaion 5)}$$

Here, *R and T* denote gas constant and temperature, respectively. KCC2 flux is driven by the difference between K^+ and Cl^- reversal potentials, V_K-V_{Cl}[27], which yields

$$J_{KCC2} = ag_{KCC2-cntr}\ln\left(\frac{[K^+]_o[Cl^-]_o}{[K^+]_{spine}[Cl^-]_{spine}}\right) \quad \text{(Equation 6)}$$

KCC2 activity coefficient is given as *a*. For example, if *a* is 0 the simulation runs with completely blocked KCC2, and if *a* is > 1, KCC2 is enhanced.

The Na/K-ATPase equation is taken from,[74] with some modification so the resting variables match electrophysiological recordings.

$$J_{Na/K-ATPase} = \frac{2 \times J_{max}}{1+exp\left(5.5 - [K^+]_o\right)} \quad \text{(Equation 7)}$$

The leakage equation is adapted such that in the resting state, concentrations are in the physiological range and no spurious drifts occur.

$$J_{leakage} = 0.05\left(125 - [K^+]_{spine}\right) \quad \text{(Equation 8)}$$

The spine intracellular Cl^- concentration $[Cl^-]_{spine}$ varies as

$$\frac{d[Cl^-]_{spine}}{dt} = \frac{J_{KCC2}}{r_{se}} \quad \text{(Equation 9)}$$

The equation for calculating the spine intracellular K^+ concentration $[K^+]_{spine}$ is:

$$\frac{d[K^+]_{spine}}{dt} = \frac{J_{KCC2}+J_{Na/K-ATPase} - J_{stimulation}}{r_{se}} + J_{leakage} \quad \text{(Equation 10)}$$

The model parameters are summarized in the Table.

Model adjustments The parameter g_{kir} was adapted to meet the mean of the peak I_{kir} observed in experiments with blocked KCC2. To achieve the 32% amplitude increase of I_{kir} between control and block of KCC2 in wet experiments $g_{kcc2\text{-}cntr}$ was adjusted. The KCC2 activity coefficient, *a*, for simulations with enhanced KCC2 was estimated to be 2, in order to achieve the 18% decrease of peak I_{kir} obtained experimentally and varied for testing the effect and consistency of KCC2 activity changes in the model.

Table of model parameters:

Parameter	Symbol	Amount	Reference
astrocyte voltage	$V_{astrocyte}$	−80 mV	clamped voltage from experiments
astrocyte K^+ concentration	$[K^+]_{astrocyte}$	135 mM	from intracellular solution used in experiments
basal conductance of astrocyte K_{i_r} channels	g_{Kir0}	6.5 nS	to match experimental results
flux capacity of KCC2	$g_{KCC2-cntr}$	5.5 mM/s	to match experimental results
temperature	T	34°C	from experiments
spine compartment volume	$Volume_{spine}$	12600 μm^3	estimated from**, 50% for spillover simulations
pECS compartment volume controlled by one astrocyte	$Volume_{ex}$	2700 μm^3	estimated from* 50% for spillover simulations
volume ratio of spine to pECS compartment	r_{se}	4.67	varied for comparison
KCC2 activity coefficient	a	0 (block), 1 (control), 2 (enhanced)	varied for comparison
pECS Cl^- concentration	$[Cl^-]_o$	129 mM	as in ASCF
maximum NA/K–ATPase flux	J_{max}	1.25 mM/s	[74]
diffusion time constant	τ_{diff}	500 ms	[75]varied for comparison

*A single protoplasmic CA1 astrocyte exclusively covers a volume of 66,000 μm^3 [76] that contains around 217800 excitatory synapses, given 330 synapses per 100 μm^3 in non-fixed acute hippocampal slices.[77] The perisynaptic volume for an 'average synapse' was assumed to be the sum of the cylindrical volume taken by a single synapse (500 nm spine diameter, 20 nm synaptic cleft,[78] and a tube-like surrounding space of 50 nm thickness and 100 nm length (based on the distance between astrocyte endfeet and synapses.[79,80] The entire pECS volume controlled by one astrocyte was estimated by multiplying the perisynaptic volume of the 'average synapse' by the number of synapses covered by this astrocyte. Note that the thus calculated perisynaptic space only is a part of the whole ECS volume fraction of 0.15–0.25[6], which additionally includes volumes lacking synaptic elements. Although the model does not directly account for the ECS complexity, it indirectly does by regarding the (peri)synaptic space as a rather distinct compartment.

**The average spine volume head in CA1 is 0.051 μm^3.[81] The spine compartment volume is a multiplication of this volume with the number of the synapses covered by one astrocyte that we calculated in *.

Local spillover modeling For modeling the spillover, pECS and spine compartments were divided each, to two equal volume compartments. Each pECS compartment was connected to one of the spine compartments, with all defined ion fluxes between these two compartments. Both pECS compartments were connected to the same astrocyte compartment. As a result, there were two full models with half the volume of the original model described in the previous sections. However, these two models share the astrocyte compartment. These two models were connected with diffusion of $[K^+]_o$, see Figure 3E (left). The diffusion equation is defined as in[75]:

$$J^i_{diff} = -J^j_{diff} = \frac{[K^+]^j_o - [K^+]^i_o}{\tau_{diff}} \quad \text{(Equation 11)}$$

The superscript number indicates which compartment the term belongs to. τ_{diff} is the diffusion time constant. Adding the diffusion term to Equation 1 yields

$$\frac{d[K^+]_o^i}{dt} = J^i_{Kir} - J^i_{KCC2} - J^i_{Na/K-ATPase} - r_{se}J^i_{leakage} + J^i_{stimulation} + J^i_{diff} \quad \text{(Equation 12)}$$

QUANTIFICATION AND STATISTICAL ANALYSIS

Astrocytic peak current was searched for at least 10 ms after last stimulation pulse. Overall charge transfer was calculated as area under the curve with start at 10 ms after last stimulation pulse and end at cross point of recorded current and pre-stimulation mean resting membrane holding current. In experiments with CNQX and DAP-5 these values were gauged with 50 ms latency after the last stimulation pulse.

The Origin 2019 software was used for statistical analysis. A Shapiro-Wilk test was used to test for a normal distribution if $n \geq 7$. In case of a normal distribution, paired Student's t tests (pTT) were used and if a significant deviation from normal distribution occurred, the non-parametric Wilcoxon signed-rank test (WSR) was used. If $n \leq 6$ WSR was used regardless of the normality test's result for paired samples. For more than 3 groups with independent samples a Kruskal–Wallis ANOVA following a Conover *post-hoc* test was used (phCT). Results with $p < 0.05$ were regarded as statistically significant. Data are presented as mean ± standard error of the mean (SEM).